Thesis for the degree
Master of Science

Submitted to the Scientific Council of the
Weizmann Institute of Science
Rehovot, Israel

עבודת גמר (תזה) לתואר
מוסמך למדעים

מוגשת למועצה המדעית של
מכון ויצמן למדע
רחובות, ישראל

By
Jonathan Reiner

מאת
יהונתן ריינר

התקן התאבכות על-מוליך על חוד עם רגישות לשדה מגנטי במישור הדגם

A SQUID on tip with in-plane magnetic field sensitivity

Advisor:
Prof. Eli Zeldov

מנחה:
פרופ' אלי זלדוב

January 2013

שבט תשע"ג

Acknowledgements

I would like to thank my supervisor Prof. Eli Zeldov for the exciting ideas that triggered this work. His constructive counsel and profound discussions made our work so interesting and satisfactory.
I thank all the lab members for their support and for creating such a pleasant working environment. In particular I wish to thank Dr. Yonathan Anahory for guiding me through every step, and for his tireless will to assist, and to Lior Embon for his generous collaboration. This work would not have been the same without their significant contribution.
I would like to acknowledge Anton Yakovenko, who contributed diligently and with much skill to the numerical work.

Abstract

Nanoscale superconducting quantum interference devices (SQUIDs) demonstrate record sensitivities to small magnetic moments, but are sensitive only to the field component which is out of the sample's plane. We report on a nanoscale three-junction Pb SQUID which is fabricated on the apex of a sharp tip. Due to its three-dimensional structure, achieved by focused ion beam processing, it demonstrates a tunable sensitivity to both in-plane and out-of-plane fields. We inspect the unique interference pattern it exhibits from both numerical and experimental point of view. This device is integrated into a scanning microscope and we present and discuss some preliminary results of magnetic imaging.

Contents

1 Introduction

The rich and diverse research on nanoscale physics gives rise to exploration of many interesting phenomena where magnetic interactions play an important role. This creates a need for precise and versatile magnetic characterization, promoting to the development of magnetic imaging techniques that concentrate on imaging small magnetic moments with high spatial resolution [1]. Among them the scanning superconducting quantum interference device (SQUID) is a promising tool due to its high sensitivity, and in particular following recent advancement in nano-SQUID fabrication [2] and SQUID measurement techniques [3, 4, 5, 6, 7, 8].

The operating principle of a SQUID is based on two properties unique to superconductivity: Cooper pair tunneling between weakly coupled superconductors, known as the Josephson Effect, and flux quantization in a superconducting ring. In such a device a dissipationless supercurrent I can flow until it reaches a critical value I_c, where the system switches to a resistive state. The I_c is a smooth and periodic function of magnetic flux Φ threading the SQUID or its pick-up loop. The measurement of I_c is a direct and precise measure of the magnetic flux in the loop.

Scanning SQUID Microscopy (SSM), as well as the other scanning probe magnetic imaging techniques, is predominately sensitive to the magnetic field component that is normal to the scanning plane [9]. In several applications such as the study of local transport currents distribution in complex samples, current-carrying edge states, transport in surface states, spin polarized currents, imaging of spin accumulation in spintronics devices, and detection of single spins with in-plane polarization the in-plane component of the magnetic field provides the more local and essential information.

Lately our group presented a novel method for fabrication of nano-SQUIDs on the apex of quartz tips that eliminated the need for complex lithography process and allows the delivery of SQUIDs-on-tips (SOTs) within several nanometers above the scanning surface [10, 11]. The above mentioned devices at the time of publication demonstrated a record sensitivity to small magnetic moments.

In this work we report yet another novel device, a three junction SQUID-on-tip (3JSOT) in a three dimensional geometric configuration [12]. The 3JSOT utilizes the benefits of this fabrication method but has a good sensi-

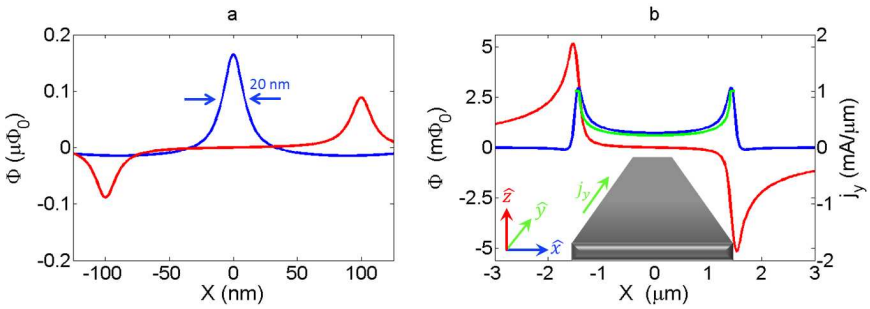

Figure 1.1: Calculated flux coupled to 3JSOT and 2JSOT due to (a) an in-plane oriented electronic spin and (b) transport current in a superconducting slab, as a function of horizontal distance. (a) The 2JSOT single-loop flux response, corresponding to the out-of-plane field H_z, results in two peaks at $\pm$100nm (red curve), whereas the 3JSOT flux difference response, corresponding to the in-plane field H_x, results in a single, centered peak with width of 20nm and a factor of two in the signal (blue curve). (b) Flux (red) and flux difference (blue) response to current density distribution $j_y(x)$ (green, secondary axis) calculated at a cross section of a superconducting slab in the Meissner state. The flux response exhibits pronounced non-local contributions and is non-vanishing only near the edges of the sample, whereas the flux difference offers excellent indication for the local current density. Both 2JSOT and 3JSOT have overall diameter of 200nm and the scanning distance is 10nm.

tivity to both in-plane and out-of-plane components of magnetic field. This sensitivity can be tuned so that the observed response will come from only one of those orthogonal components or from their combination.

The 3JSOT operation principle incorporates two main ingerdients. The double-loop gradiometric design makes the device responsive not only to the flux threading each loop, Φ_L and Φ_R, but also to their sum and difference, $\Phi^+ = \Phi_L + \Phi_R$ and $\Phi^- = \Phi_L - \Phi_R$. In addition, a special three-dimensional structure associates Φ^+ to the out-of-plane field, denoted by H_z, and Φ^- to the in-plane field, denoted H_x. In order to highlight the advantages of our novel device, we will consider two generic case studies.

Imaging an in-plane oriented single spin

The dashed red curve in Fig. 1.1a shows the spatial flux response of a 2JSOT, 200 nm in diameter, due to an in-plane spin located at X=0, assuming working distance $d = 10nm$. Sensitivity to the normal magnetic flux density lines H_z dictates that the coupling is strongest where the SOT circumference is right above the spin [5, 7, 13]. This nontrivial response function is problematic for the purpose of imaging, since it requires deconvolution procedure that will ultimately degrade spatial resolution. On the other hand, sensitivity to the in-plane field H_x conveniently implies strongest

response when the SQUID is centered right above the spin. Therefore, tuning the 3JSOT to be mainly sensitive to the flux difference Φ^-, contributed by the in-plane field, enhances the resolution. Moreover, this combination of flux accumulate opposite sign for Φ_R and Φ_L, thus giving rise to twice the signal in Φ^- for the same overall diameter, as demonstrated by the solid blue line in Fig. 1.1a.

Studying the distribution of a local transport current

In the second case study we consider a thin sample carrying an inhomogeneous sheet current density in the $\hat{y}$ direction, $J_y(x)$. The contribution to the in-plane field $H_x(x_0)$ due to a current element at x_0 is just $\frac{J_y(x_0)}{2}\mathrm{d}x$, thus, at close proximity to the surface $H_x(x)$ is just proportional to the local current density. As opposed to that, the local current density contribution to the out-of-plane field $H_z(x)$ vanishes, giving rise to a very non-local dependence. A good realization of this is the measurement of a transport current in a superconducting slab in the Meissner state [14], as demonstrated in fig. 1.1b. The Current density can be extracted from the in-plane field in a straightforward manner, whereas existing scanning probe techniques, which currently measure only the out-of-plane field, require elaborate nonlocal inversion schemes [15, 16]

2 Theory

2.1 Superconductivity

Superconductivity is a phase of matter that was first observed in 1911 by H. K. Onnes in Leiden [17]. The two main hallmarks of this phase are perfect conductivity, where the resistance of the material drops sharply to zero at the transition temperature T_c, and perfect diamagnetism, also known as the Meissner effect, in which the superconductor expels any magnetic field from its interior. A description of these electrodynamic properties was formalized in 1935 by the London brothers by introducing two equations for the electric and magnetic fields. These equations indicate an exponential screening of the expelled field with a characteristic length scale: [18]

$$\lambda_L\left(T=0\right)=\left(\frac{mc^2}{4\pi ne^2}\right)^{1/2} \tag{2.1}$$

Where m is the mass, e is the electron charge and n is the conduction electron density. λ_L has been empirically shown to be temperature dependent:

$$\lambda\left(T\right)\approx\lambda\left(0\right)\left(1-\left(\frac{T}{T_c}\right)^4\right)^{-1/2} \tag{2.2}$$

The Ginzburg-Landau Theory

A major theoretical advancement was achieved in 1950 by Ginzburg and Landau within their general theory of second-order phase transitions. They treated the superconducting condensate by introducing a complex pseudo-wavefunction ψ as an order parameter. This theory was somewhat disregarded at first, due to its phenomenological approach. However, in 1959 it was shown by Gor'kov that it is, in fact, a limiting form of the more celebrated microscopic theory of BCS, valid near T_c. A significant physical interpretation can be assigned to the order parameter, given that the local density of superconducting electrons is $|\psi|^2=n_s$, by the following argument. If we substitute $\psi=\sqrt{n\left(\mathbf{r}\right)}e^{i\theta(\mathbf{r})}$ into the probability current derived from

the Schrödinger equation

$$\mathbf{J} = \frac{1}{2m}\left(\psi^*\left(\frac{\hbar}{i}\nabla - q\mathbf{A}\right)\psi + h.c.\right) \tag{2.3}$$

and then arrange the terms and multiply by the charge q, we obtain

$$\mathbf{J} = qn_s\frac{\hbar}{m}\left(\nabla\theta - \frac{q}{\hbar}\mathbf{A}\right) \tag{2.4}$$

In the case of a condensate this is simply the electric current, and comparing this to the expression $\mathbf{J} = qn_s\mathbf{v}$ we can recognize the kinetic momentum

$$m\mathbf{v} = \hbar\nabla\theta - q\mathbf{A} \tag{2.5}$$

Thus, we can assign the phase θ to the center-of-mass motion (or the p-momentum) of the superconducting electrons. Apart from the penetration depth, another characteristic length that emerges from the GL theory is the coherence length ξ, which characterizes the distance over which $\psi(\mathbf{r})$ decays near the edge of the superconductor.

The BCS Theory

In 1957 Bardeen, Cooper and Schrieffer (BCS) published their work which attributes superconductivity to a weak attractive interaction between electrons, mediated by second-order electron-phonon interaction. This attractive interaction gives rise to pairing of electrons with spatial extension of the order of ξ which constitute a composite boson. The so called Cooper-pairs can therefore form a condensate which is described by a collective wavefunction. The theory predicts the opening of an energy gap which is related to the amount of energy required to break a pair. As a result, excitations with energy smaller than the gap, such as electron scattering, are forbidden and superconductivity is established.

Type I and Type II Superconductors

Expulsion of the magnetic field from the interior of the superconductor is energetically favorable only up to some critical field H_c. Above H_c, or above the corresponding critical current density j_c, superconductivity is destroyed, allegedly in a sharp discontinuous transition to the normal phase. In 1957 Abrikosov argued that the recovery of the normal phase can happen in a rather different manner. He classified superconductors using the ratio of the two characteristic lengths $\kappa = \frac{\lambda}{\xi}$, and argued that for superconductors with $\kappa > \frac{1}{\sqrt{2}}$, negative surface energy between normal and superconducting domains gives rise to a mixed state. Namely, above a lower critical field H_{c1}, flux can penetrate through domains shaped like tubes with normal cores and

encircled by a vortex of supercurrent. Only at a higher critical field H_{c2} the sample becomes completely normal. It was already found earlier, following a Bohr-Sommerfeld like quantization argument, that the flux penetrating through a hole (or normal region) in a superconductor should be an integer number of the magnetic flux quantum

$$\Phi_0 = \frac{h}{2e} = 2.07 \times 10^{-7} \frac{G}{cm^2} \tag{2.6}$$

The result is the formation of the vortex phase, where flux tubes, each carrying one flux quanta interact and arrange in a regular array. This phenomena, also known as Abrikosov lattice, was observed in 1967 by means of magnetic decoration and electron microscopy [19].

2.2 The Josephson Effect

The tunneling current of cooper pairs between weakly coupled superconductors, i.e. superconductors separated by a thin barrier, was predicted by B. D. Josephson in 1962 [20]. We will present a simplified derivation of it due to Feynman [21]. The time evolution of the wave functions of two superconductors separated by a thin insulator can be written as:

$$\begin{aligned} i\hbar \frac{\partial \psi_1}{\partial t} &= U_1 \psi_1 + K \psi_2 \\ i\hbar \frac{\partial \psi_2}{\partial t} &= U_2 \psi_2 + K \psi_1 \end{aligned} \tag{2.7}$$

Here ψ_i is the collective Ginzburg-Landau wave function of the condensate:

$$\begin{aligned} \psi_1 &= \sqrt{n_1} e^{i\theta_1} \\ \psi_2 &= \sqrt{n_2} e^{i\theta_2} \end{aligned} \tag{2.8}$$

U is the energy and K is the coupling energy between the superconductors, which is a property of the particular junction and allows the tunneling. Suppose we connect the two electrodes to a battery and apply voltage V across the junction. Then $U_1 - U_2 = 2eV$, and for convenience we can define the zero energy to be halfway between. Substituting (2.8) into (2.7), equating the real and imaginary parts and letting $\delta = \theta_2 - \theta_1$ yields

$$\begin{aligned} \dot{n}_1 &= +\frac{2}{\hbar} K \sqrt{n_1 n_2} \sin \delta \\ \dot{n}_2 &= -\frac{2}{\hbar} K \sqrt{n_1 n_2} \sin \delta \end{aligned} \tag{2.9}$$

$$\begin{aligned} \dot{\theta}_1 &= +\frac{K}{\hbar} \sqrt{\frac{n_2}{n_1}} \cos \delta - \frac{2eV}{2\hbar} \\ \dot{\theta}_2 &= +\frac{K}{\hbar} \sqrt{\frac{n_1}{n_2}} \cos \delta + \frac{2eV}{2\hbar} \end{aligned} \tag{2.10}$$

Consider equation (2.9), we recognize an opposite change rate of the charge carriers densities $\dot{n}_1 = -\dot{n}_2$, which implies a flow of current. Hence, if we denote $j_0 = \frac{2K}{\hbar}\sqrt{n_1 n_2}$, and integrate the current through the whole cross-section of the junction we find the DC Josephson relation:

$$I_s = I_c \sin(\gamma) \tag{2.11}$$

Here I_c is the maximal supercurrent the junction can support and we introduce the gauge-invariant phase difference, necessary in the presence of a magnetic field

$$\gamma = \delta - \left(\frac{2\pi}{\Phi_0}\right) \int \mathbf{A} \cdot \mathrm{d}\mathbf{s} \tag{2.12}$$

This implies that a DC current can flow through the junction even in the absence of electromagnetic field. However, this current may depend on the magnetic flux through the junction, as indicated by the vector potential term.

When we take into account the applied voltage V, equation (2.11) still holds, but n_1 and n_2 do not in fact change, they remain constant and equal to n_0. By subtracting the two equations in (2.10) we find the time dynamics of the phase difference, known as the AC Josephson relation:

$$\dot{\delta} = \frac{2eV}{\hbar} \tag{2.13}$$

That is, applying DC voltage on the junction induces AC current at a frequency $\frac{2e}{\hbar}V$.

2.3 DC SQUID

A DC SQUID consists of a superconducting ring interrupted by two Josephson junctions. The junctions can be realized by an insulator (SIS) or normal metal (SNS) layer, or by geometrical constriction (Dayem bridge). We can use Stokes' theorem to calculate the flux enclosed within the ring in terms of the vector potential.

$$\Phi = \int (\nabla \times \mathbf{A}) \cdot \mathrm{d}\mathbf{s} = \oint \mathbf{A} \cdot \mathrm{d}\mathbf{l} = \left(\frac{\Phi_0}{2\pi}\right) \int\limits_{electrodes} \nabla\theta \cdot \mathrm{d}\mathbf{l} + \int\limits_{links} \mathbf{A} \cdot \mathrm{d}\mathbf{l} \tag{2.14}$$

The third equality is a consequence of splitting the integration contour. Then we can use the G-L relation $m^*\mathbf{v}_s = \hbar\nabla\theta - \frac{2e\mathbf{A}}{c}$, assuming that the contour is taken inside the superconductor where $\mathbf{v}_s = 0$, to replace $\mathbf{A}$ with the phase gradient. As θ is single-valued, the integral over the whole contour should be zero modulo 2π, so we can replace the term $\int\limits_{electrodes} \nabla\theta \cdot \mathrm{d}\mathbf{l}$ with

the phase differences accumulated across both junctions $\delta_1 - \delta_2 \ \ (mod 2\pi)$. Combining that with (2.12) we obtain:

$$\gamma_1 - \gamma_2 = \frac{2\pi\Phi}{\Phi_0} \ \ (mod 2\pi) \tag{2.15}$$

The supercurrent through the SQUID itself is the sum of the supercurrents through the junctions, where we assume $I_{c_1} = I_{c_2} = I_c$ for simplicity, thus:

$$I = I_c \left(\sin\left(\gamma_1\right) + \sin\left(\gamma_2\right)\right) \tag{2.16}$$

Combining equations (2.15) , (2.11) and using trigonometry, one can show that the maximal current is:

$$I_{max} = 2I_c \left|\cos\left(\frac{\pi\Phi}{\Phi_0}\right)\right| \tag{2.17}$$

Equation (2.17) demonstrates the ability of the SQUID to measure Φ up to a very small fraction of Φ_0, and thus be used as a very sensitive magnetometer. This behavior imposes a straightforward analogy to the celebrated two-slit experiment, where the junctions play the role of the slits as the agent for the phase interference.

3 Methods

3.1 Fabrication

3.1.1 Tip Processing

The first step in the fabrication of a SOT is pulling a tube to sub-micron dimensions. We use capillaries made of borosilicate glass with a θ-shaped cross section (OD=1mm, ID=0.7mm) and an industrial pulling machine, Sutter Instrument Co. P-2000 Micropipette Puller. The capillary is heated by laser and subsequently pulled to form two tips with sharp apex, while preserving its θ-shaped cross section. The final size of the apex is controlled by the exact pulling parameters, and can have an overall diameter as small as 200 nm. Two 200 nm thick Au contacts are evaporated along the tube, and a mask with an opening 10 mm long and 0.3 mm wide is used to prevent an overlap between them. The tips are then subjected to a Focused Ion Beam (FIB) nano-machining process in an Helios 600 FIB/SEM Dual Beam Microscope. The apex is milled to a V shape at some desired angle, so that the central partition protrudes forward (see Fig. 3.2a). The process is carried out as following:

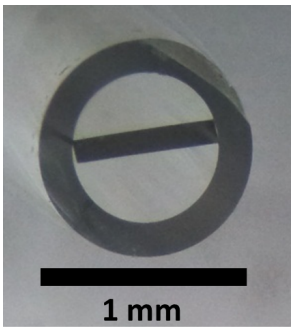

Figure 3.1: θ-tip. An optical microscope image of a tip with θ cross section.

1. The tip is positioned in the vacuum chamber normal to the ion beam direction and the apex is brought to the eucentric point while keeping the central partition of the θ aligned with respect to the ion beam.

2. On a snapshot image of the FIB, the milling segments are specified to obtain the V shape cut and a milling beam, 7-12 nm in diameter, is activated.

3. The resulting cut is inspected by another FIB snapshot and by the SEM beam (giving complementary image from a different point of view, tilted by 52°with respect to the FIB), and corrected if necessary.

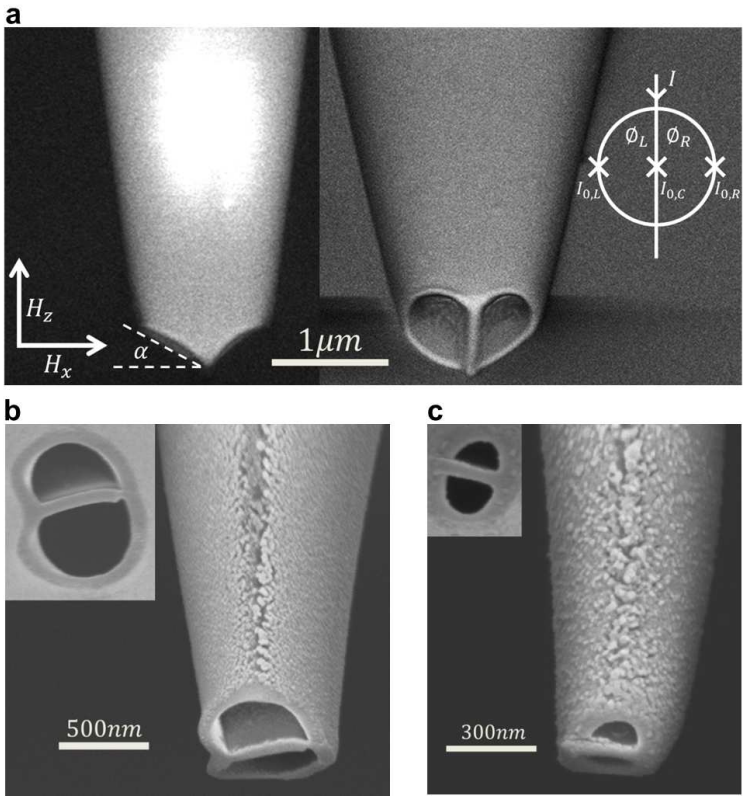

Figure 3.2: Scanning electron microscope images of a tapered θ-tip and 3JSOT devices. (a) SEM images of a bare borosilicate θ-tip after patterning. The magnetic field orientation and the tapering angle α are denoted. The inset shows schematic diagram of the 3JSOT. (b) A 3JSOT with effective loop dimension of $A = 0.45\mu m^2$ ($A_1 = 0.27\mu m^2$ and $A_2 = 0.18\mu m^2$). The two Pb deposited electrodes and the gap that forms the side junction are clearly seen. (c) A 3JSOT with effective loop dimension of $A = 0.077\mu m^2$ ($A_1 = 0.04\mu m^2$ and $A_2 = 0.037\mu m^2$).

3.1.2 Tip Deposition

The SOT geometry requires the formation of two superconducting electrodes that are separated by an insulating gap and overlap the Au contacts. In addition, a superconducting ring has to be deposited on the apex, or on the θ cross section in the case of the 3JSOT. The ring has narrow parts due to the gap between the two leads, and these parts form the SOT's weak links. In the 3JSOT, the additional weak link is formed by the central bridge of the θ. Providing these conditions necessitated the development of a self-aligned deposition scheme including in-situ rotation [10], as illustrated in Fig. 3.3. In the first and second steps, the θ-tip is tilted in $\pm 110^\circ$ respectively, and 15-18nm thick Pb layers are evaporated on the sides, forming the electrodes.

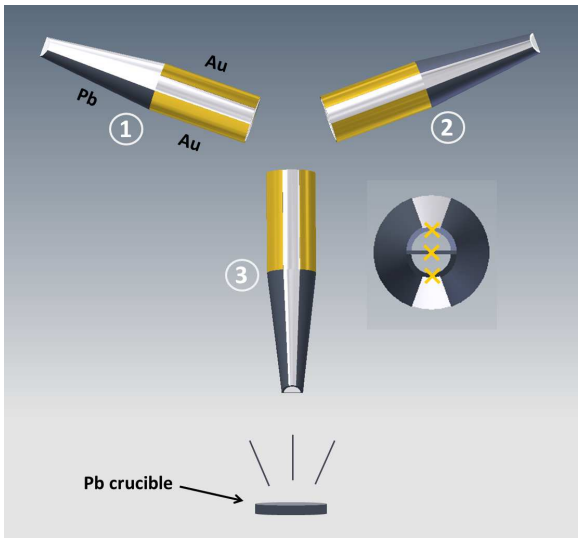

Figure 3.3: Schematic diagram of the three-step deposition scheme applied to fabricate SOTs. In steps 1 and 2 the side contacts are evaporated, and the ring in step 3. The inset shows a point of view projected from the 3JSOT apex, stressing out the SQUID geometry of the device.

On the third step, 10-12nm thick layer is evaporated on the apex to form the ring. During all three steps the average deposition rate is 0.5 $^{nm}/_{s}$. This scheme requires careful design of a suitable tip holder and proper adjustment in the thermal evaporator, both carried out by lab members in several stages prior to this work. We will describe briefly the present condition of these aspects, used for our device.

Tip Holder

In Fig. 3.4 a model of the tip holder is presented. The two ends of it are designed as a male 'dovetail' adapter and are used to attach the holder easily and firmly. This adapter is electrically isolated in order to have the holder floating with respect to any female adapter in use. The tip is fixed in a circular groove, and electrical contact to the Au electrodes is established by two BeCu springs pressing the tip from both sides. One spring is attached to the top contact, while the other

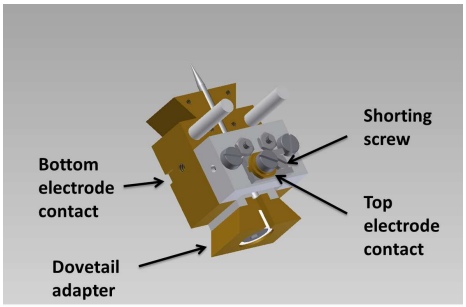

Figure 3.4: Tip holder

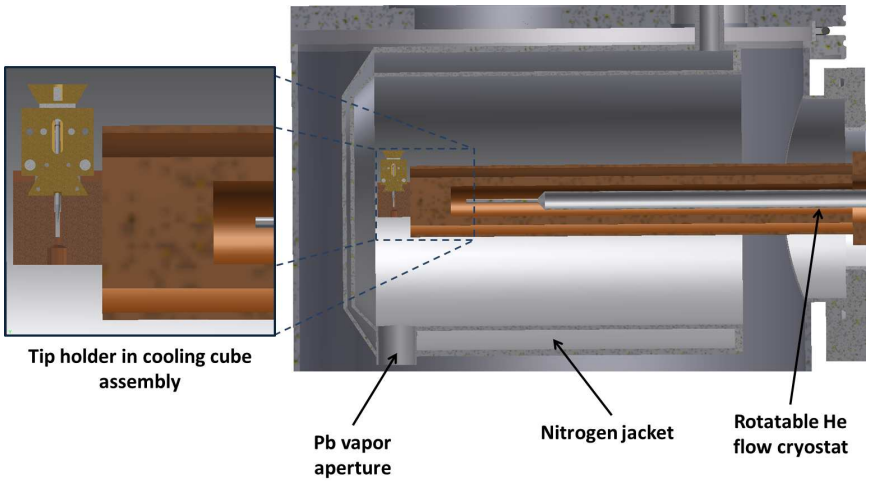

Figure 3.5: ^{4}He flow cryostat and evaporation chamber assembly

is attached to the body of the holder. A small screw on the top contact enables to short between the two electrodes while not measuring, in order to detach the SQUID from the external circuit and protect it from electrostatic discharge. The tip protrudes $\sim$ 3mm from the holder to allow deposition and scanning.

Evaporation Chamber

The high surface mobility of Pb induces island growth and poor adhesion. This in turn prevents the creation of thin uniform films necessary for the formation of the leads and ring. To overcome this problem a technique for thermal evaporation in cryogenic temperatures was developed. An in-situ rotatable ^{4}He flow cryostat is enclosed within a liquid nitrogen jacket inside a vacuum chamber in a base pressure of 2×10^{-7} Torr. The tip is thermally coupled to the cryostat through the holder and by a brass cooling cube which surrounds the protruding part. This configuration is presented in Fig. 3.5. To enhance thermal conductivity before and in between the depositions, ^{4}He is introduced into the chamber as exchange gas, raising the pressure to 5×10^{-6} Torr and its flow is interrupted during the depositions.

3.2 Probe and Electronics

SQUID Series Array Amplifiers (SSAA) and Custom Electronics

The SSAA is used as a cryogenic, low-impedance current-to-voltage convertor [22] for the 3JSOT current. It consists of a hundred Nb SQUIDs

connected in series , which are inductively coupled to the 3JSOT branch and to a feedback coil. A change in the 3JSOT current induces a change in the magnetic flux of the SSAA and in its critical current and voltage accordingly, which is amplified by the pre-amplifier box. The SSAA is operated in a flux-locked loop mode (FLL).

Measurement Circuit

The operation of the 3JSOT is based on a quasi-voltage bias configuration. Schematics of the circuit and several IV curves are shown in Fig. 4.2. The shunted SQUID is current biased by sweeping the applied voltage V_b connected in series to a cold $R_b \cong 5\text{k}\Omega$ resistor up to the critical current when the normal state starts to form. As the SQUID becomes resistive, current flows also through the shunt resistor $R_s \cong 1\Omega$, and as the SQUID resistance increase, it becomes effectively voltage biased. The 3JSOT current I_{3J} is converted and amplified by the SSAA which is inductively coupled to the 3JSOT. The amplified signal is fed into the feedback box and a voltage V_{FB} is supplied to the feedback coil in order to compensate for the change, so that V_{FB} is proportional to I_{3J}. Once the current starts to flow through the shunt resistor, one detects decreasing V_{FB}, and thus a maxima in the IV curve corresponding to the critical current of the 3JSOT. The decreasing current in the 3JSOT for increasing V_b results in a negative differential resistance, which is an essential ingredient for imaging purpose.

3.3 Scanning Microscope

A 4 K Scanning SQUID Microscope (SSM) adjusted to SOTs was developed and built in our lab. The SSM also incorporates atomic force microscopy (AFM) abilities when a tuning fork is attached to the tip. The microscope resides in a vacuum cap at the bottom of a rod, to be inserted into a Helium dewar, and various electrical connectors are wired through the rod to its top part. A stack of commercial Attocube piezoelectric coarse positioners and scanners enables three-dimensional positioning with nanometric precision within a volume of the order of a few mm. The sample holder is connected at the bottom of the positioner stack. It incorporates, in addition to the chip carrier with electric contacts, a calibrated Lakeshore diode and a heater for temperature control of the

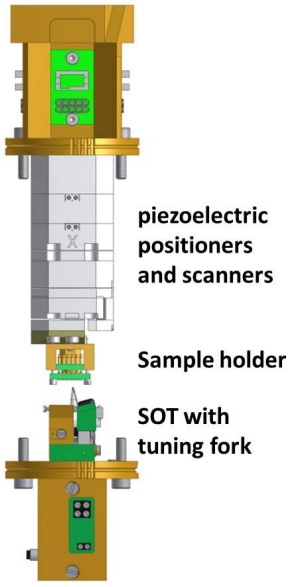

Figure 3.6: Schematic view of the SSM assembly

sample. In this design, it is the sample which is moved in respect to the stationary tip. The SOT is situated opposite the sample at the bottom part of the rod. This part also holds the electronics required for the tuning fork operation. A schematic view of the SSM assembly is showen in Fig. 3.6.

4 Results

4.1 I_c Interference Pattern

Numerical Simulations

In order to inspect the properties of our device, numeric simulations in MATLAB were carried out. The first goal was to reconstruct the interference pattern of the critical current I_c of the new device. in order to do that we can generalize equation (2.15) to the three-junction case, by considering each sub-loop as a separate SQUID. We also need to take into account that the total flux in the loop is a sum of the applied flux and the flux induced by the circulating current.

$$\begin{aligned}\delta_L - \delta_C &= \frac{2\pi}{\Phi_0}\left(\Phi_L^a - L_L I_{0,L}\sin\delta_L + L_C I_{0,C}\sin\delta_C\right) \pm 2\pi \\ \delta_C - \delta_R &= \frac{2\pi}{\Phi_0}\left(\Phi_R^a - L_C I_{0,C}\sin\delta_C + L_L I_{0,L}\sin\delta_R\right) \pm 2\pi\end{aligned} \tag{4.1}$$

The subscripts L,R and C denote respectively the left, right and central arm of the 3JSOT. Φ^a is the applied flux, δ is the phase difference across the junction, I_0 is its critical current and L is the inductance (see schematics inset in Fig. 3.2). We now consider the total current, which is a function of the phase differences given by:

$$I_{total} = I_{0,L}\sin\delta_L + I_{0,C}\sin\delta_C + I_{0,R}\sin\delta_R \tag{4.2}$$

Upon setting Φ_L^a and Φ_R^a, we can use (4.1) to eliminate two phases from (4.2) and finally find the maximal I_{total} which defines the device's I_c. This problem can be treated numerically, and for our purpose it is illuminating to define the flux sum $\Phi^+ = \Phi_L^a + \Phi_R^a$ and difference $\Phi^- = \Phi_L^a - \Phi_R^a$, which are significant physical quantities in this configuration. The resulting pattern $I_c(\Phi^+, \Phi^-)$ is a periodic lattice of triangular peaks (Fig. 4.2), where their exact shape is subjected to the critical current and inductance parameters (see Fig. 4.1). As in the 2JSQUID case, the critical current affects the amplitude of the modulation, whereas the inductance mainly governs its depth. We can also introduce asymmetry factors into the calculation, and inspect their influence on the pattern.

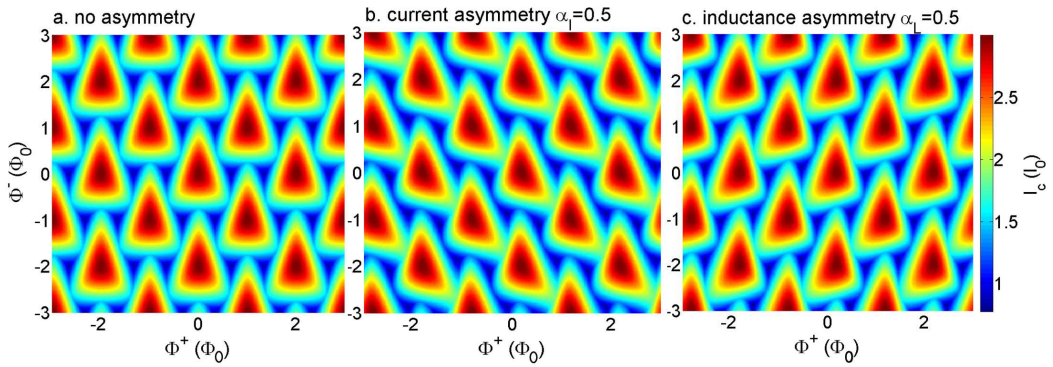

Figure 4.1: $\mathbf{I_c}\,(\mathbf{\Phi}^+, \mathbf{\Phi}^-)$ in symmetric and a asymmetric configurations. (a) No asymmetry is introduced. (b) Current asymmetry is introduced. Here we assign $I_{0,L} = I_{0,C}\,(1+\alpha_I)$ and $I_{0,R} = I_{0,C}\,(1-\alpha_I)$, where $\alpha_I = 0.5$ and $I_{0,C}$ is chosen to be some average typical critical current. (c) Inductance asymmetry is introduced. Here we assign $L_L = L_C\,(1+\alpha_L)$ and $L_R = L_C\,(1-\alpha_L)$, where $\alpha_L = 0.5$ and L_C is chosen to be some average typical inductance.

Consider the maxima in I_c: initially it corresponds to some specific value of the applied flux. By introducing asymmetry we modify the circulating currents and thus the total flux, therefore shifting the pattern as a whole along the flux axes. This effect can be advantageous in practice, because shifted patterns give rise to wider range of sensitive points when using both polarities of bias current. In addition, as a consequence of the asymmetric weight of the actual Φ_R and Φ_L the triangles deform and the interference pattern appears skewed. The result is that negative and positive slopes along a vertical or horizontal flux cross-section are no longer symmetric around their extrimum. We conclude this part of the discussion by presenting a few examples of the above mentioned trends and pointing out the analogy to the 2JSQUID case (see Ref. [23], section 2.2.4).

To use the 3JSOT as a magnetometer in practice, we have to associate its geometry with the applied magnetic fields and represent I_c as a function of H_z and H_x. For a 3JSOT with tapering angles α_L and α_R ($\alpha \neq 0$ to avoid singularity) and loop effective areas A_L and A_R, the fields are associated with the flux by applying the following transformation:

$$\begin{pmatrix} H_z \\ H_x \end{pmatrix} = \frac{1}{A\,(1-\Delta^2)\sin\alpha} \begin{pmatrix} \tan\alpha & -\Delta\tan\alpha \\ \Delta & -1 \end{pmatrix} \begin{pmatrix} \Phi^+ \\ \Phi^- \end{pmatrix} \tag{4.3}$$

Where we have defined $A = A_L + A_R$, $\Delta = \frac{A_L - A_R}{A}$ and $\alpha = \alpha_L = \alpha_R$[1]. Note that the off-diagonal terms scale like Δ so for a nearly symmetric 3JSOT

[1]We only assume that for the sake of clarity, as the transformation takes a more instructive form. In practice we do take angle asymmetry into consideration.

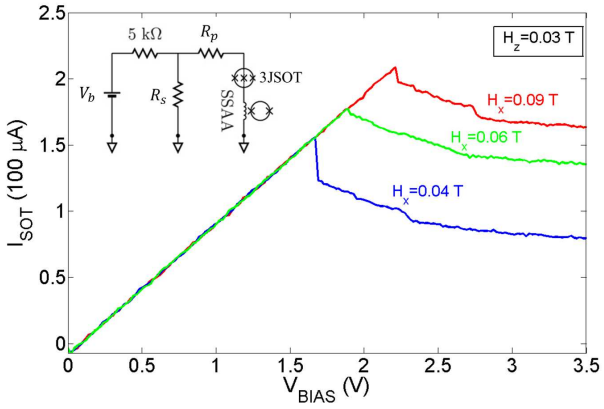

Figure 4.2: I-V curves. The plot shows several curves at different H_x field biases indicated above the curves, at constant $H_z = 0.03$T. The critical current corresponds to the maximum and is followed by the negative differential resistance regime. The inset shows schematics of the measurement circuit.

($\Delta \ll 1$) H_z corresponds, up to a factor, to Φ^+ and H_x corresponds to Φ^-, as we would expect from the geometry. This transformation implies yet another non-trivial modification of the interference pattern, this time subjected to the geometrical parameters A, Δ and α. However, these parameters show a more pronounced impact on the pattern, as they affect not merely individual triangles or an overall shift, but also modify the structure of the lattice itself, i.e changing its periodicity and directionality (see fig. 4.3). This fact suggests that the geometrical parameters can be extracted from the pattern by a 2D Fast Fourier Transform (2DFFT) with respect to the fields, in a similar manner to the way we determine the effective area of a 2JSQUID by the oscillation period. This suggestion was verified self-consistently by performing 2DFFT of the simulation results and recovering the predetermined parameters. The 2DFFT is a powerful tool since it is robust to the particular deformation of an individual triangle, and we used it to narrow substantially the large parameter space we scan in order to fit the data.

Measurements

The characterization process of a 3JSOT is a long process as it requires a high resolution scan of three parameters: bias voltage and two applied fields. For each field bias we recorded the I-V curve as described in section 3.2 in order to extract the critical current. In Fig. 4.2 I-V curves for three different applied fields are plotted. We used a MATLAB generated code to spot the exact I_c on the curve. In principle this is an easy task, since it is supposed to correspond to the maximum of the curve. However, we

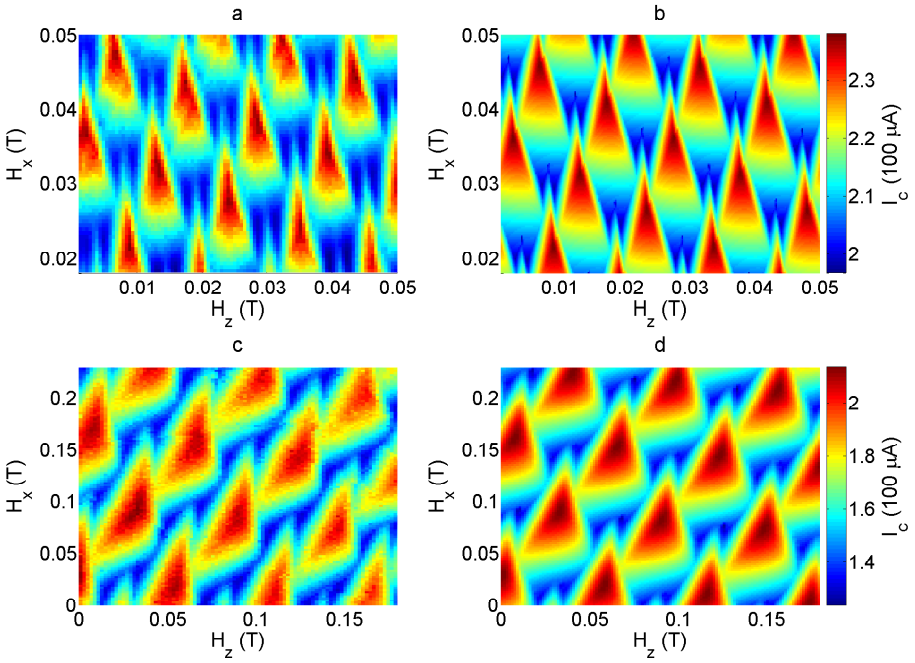

Figure 4.3: 3JSOTs interference pattern. (a) measurement and (b) simulation of $I_c(H_x, H_z)$ of the $0.45\mu m^2$ 3JSOT. The orientation of the triangles lattice is subjected to the geometrical structure. (c) measurement and (d) simulation of $I_c(H_x, H_z)$ of the $0.077\mu m^2$ 3JSOT.

sometimes encountered difficulties due to instability of the SSAA near the critical point that induce jumpiness of the data curve. As we shall see, this is a more general and severe problem when it comes to imaging, and it is currently being addressed in the lab. In the context of characterization it implies that we had to develop algorithms that detect the spot by the change in the derivative to obtain reliable results.

Figure 4.3 shows the measured $I_c(H_z, H_x)$ of two 3JSOTs, and the corresponding simulation fits. The interference pattern in Fig. 4.3a is obtained from the device imaged in Fig. 3.2b, and the pattern in Fig. 4.3c from the device in Fig. 3.2c. For clarity we will denote them by their overall loop area, $0.45\mu m^2$ and $0.077\mu m^2$, respectively. In order to fit the data we begin by performing FFT, extracting the geometrical parameters and comparing it to the SEM images. As an example, FFT of the $0.077\mu m^2$ 3JSOT is shown in Fig. 4.4. Since the FFT is with respect to H_z and H_x, the axes were scaled by Φ_0 to obtain dimensions of area. Two symmetric pairs of peaks are identified and the area and tapering angle are given by the coordinates of the position vector to the corresponding peak (in a polar basis). To enhance the resolution and accuracy the FFT was performed on a data

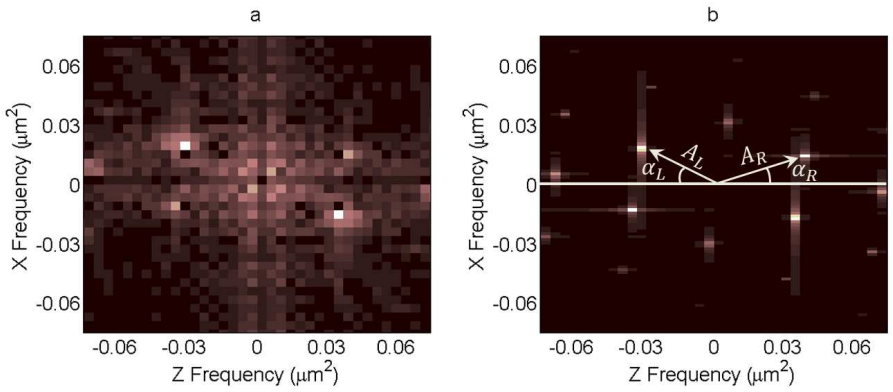

Figure 4.4: 2D FFT of the 0.077μm^2 3JSOT. (a) Data, based on all four quadratures. (b) Simulation, taking into account more periods to gain higher resolution. The arrows indicate the locations of the maximas and the quantities derived from them.

set that contains all four quadratures. The orientation (left or right) has, of course, no real geometric meaning and is used here just as a convenient notation. This concept is illustrated diagrammatically in the figure, and the derived values are $A_L = 0.04\mu\text{m}^2$, $A_R = 0.037\mu\text{m}^2$, $\alpha_L = 19°$ and $\alpha_R = 27°$. These values agree with the SEM images, i.e. they fall in the range of areas given by taking into account the finite width of the tip circumference. The maximal total current of this 3JSOT is $I_c = 210\mu\text{A}$. We also deduced from the simulations that the modulation depth depends on the critical current and inductance. This is equivalent to the two-junction case, where the StewartMcCumber parameter, $\beta_L = \frac{2LI_0}{\Phi_0}$ governs the modulation depth. Thus, knowing the modulation depth - 38% in this case, we could find the total inductance - $L = 45\text{pH}$. In Fig. 4.5 we compare data versus simulation by taking a horizontal cross section of Fig. 4.3 c and d. The mismatch near the minimas reflects an error in fitting of the individual triangle orientation, which could also be noticed in the color plots.

The numbers for the $0.45\mu\text{m}^2$ 3JSOT are $A_L = 0.27\mu\text{m}^2$, $A_R = 0.18\mu\text{m}^2$ and $\alpha = 22°$. The larger critical current $I_c = 240\mu\text{A}$ is probably due to its bigger size. Decreased modulation depth of 15% implies larger inductance - $L = 70\text{pH}$, potentially increasing the flux noise. Using the above mentioned numbers (with some tolerance) to decrease the parameter space, we scanned the fitting parameters. Then we assigned each fit an index corresponding to its $\mathcal{L}^1$ metric with respect to one unit-cell of the data. The best fits are presented in Fig 4.3 b and d. Fitting also allows us to probe into the subloop structure. In the first 3JSOT we find that $\sim 50\%$ of the maximal current flows through the central junction, $\sim 40\%$ through one of the side junctions and only $\sim 10\%$ through the remaining junction. In the second 3JSOT

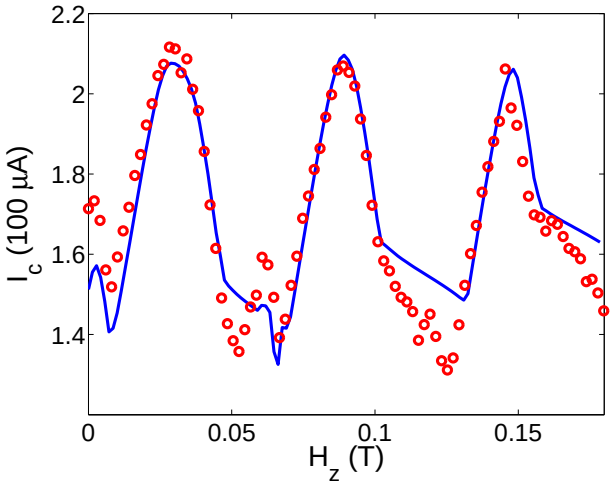

Figure 4.5: Cross Section of the $0.077\mu m^2$ 3JSOT data (red circles) and simulation (blue curve) at $H_x = 0.085T$.

almost 60% flows through the central junction, $\sim$ 25% through one of the side junctions and $\sim$ 15% through the other. Remarkably, the inductance distribution has the opposite trend. The contribution of the central branch to the total inductance is only $\sim$ 20% in the first device, $\sim$ 10% in the second device, and the rest is distributed equaly between the two side branches in both cases. Thess findings may indicate that the effective width and thickness of the central Dayem bridge is larger, naturally giving rise to higher critical current. Regarding the inductance, we suppose that in a device of such small dimensions, it is goverened mainly by the kinetic inductance, $L_k = \frac{\mu_0 \lambda_L^2 l}{wt}$, where l is the bridge length, t is the film thickness and w is its width. Thus, a wider and thicker structure implies smaller contribution to the total inductance. Indeed, the central junction appeares to be wider in SEM images, and it is definitley thicker because its plane is perpendicular to the direction of the deposition beam, whereras the planes of the side junctions are tilted with respect to this direction.

4.2 Scanning Microscopy

After gaining confidence in the fabrication and characterization of the device, we aimed towards integrating it into the 4K SSM. Currently, this is still an ongoing project, so we shall discuss only some aspects we have encountered so far.

4.2.1 Scanning Conditions

Field Sensitivity

To measure the change in the field, we voltage-bias the 3JSOT and measure the corresponding V_{FB}. Since I_c changes as a function of field, the negative differential resistance part of the I-V curves shifts, and in this region V_{FB} becomes a function of the field. We consider biases where this function is smooth and linear as sensitive points and define the sensitivity as $\frac{\Delta V_{FB}}{\Delta H}$. This implies that apart from the modulation depth, a smooth and moderate negative differential resistance is desired to ensure considerable sensitivity. Clearly we must find proper working points per applied field bias to obtain a device which operates at wide range of fields. However, this is not always the case. Instabilities in the measurement circuit induce jumpiness of the I-V curves at the critical point which is manifested in the absence of negative differential resistance, and severely restrict the operation range.

Field Decoupling

To realize a practical magnetometer out of the 3JSOT, decoupling of the response function to in-plane and out-of-plane fields must be feasible. One approach would be to apply such external magnetic fields and voltage bias at which the gradient is large in one direction and vanishes in the other, i.e the contour lines in the $I_c(H_x, H_z)$ plot are parallel to one of the axis (see Fig 4.6). To gain a more quantitative measure, it is convenient to define the decoupling ratio in the vicinity of a working point: $\frac{\Delta V_{FB}/\Delta H_i}{\Delta V_{FB}/\Delta H_j}$, with $i, j = x, z$. It is self-evident that properties of such a decoupling regime are subjected to the specific details of the interference pattern, which can be manipulated only to some extent in the fabrication process. The practical implementation of such a controlled manipulation should be studied more thoroughly. We can generally state, however, that a symmetric device is desired since it preserves orthogonality and symmetry of the interference pattern (see Fig. 4.1 and equation (4.3)), and thus assures in-plane sensitive regions, which are the key ingredient of the 3JSOT. Alternatively, to reduce this restrictive dependency on the specifics of the device, a different approach can be adopted. Acquisition of the response in two different applied fields configurations, which results in two linearly independent gradients, can be used to diagonalize the signal. Namely, the in-plane and out-of-plane picture can be reconstructed from a linear combination of two mixed signals, measured at a predetermined working points.

Dynamic Working Range

The necessity of applying external field bias to operate a device which measures magnetic fields raises an intrinsic limitation. In such conditions, it is

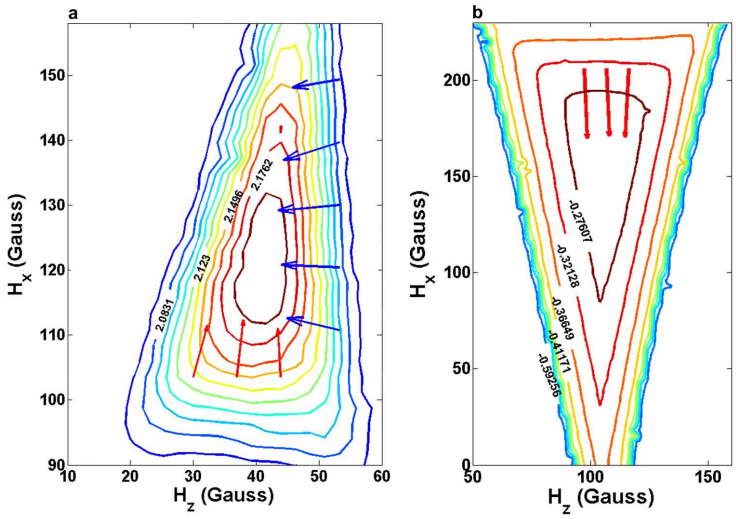

Figure 4.6: Contour plots of field-biased dynamic working regime of two different devices. The contour line labels denote the feedback voltage response (in volts) , and the arrows represent its normalized gradients, with a typical magnitude of a few millivolts per gauss. (a) Two complementary regimes are identified: one sensitive mainly to H_x, marked by the red arrows and nearly horizontal contour lines, and one sensitive mainly to H_z, marked by blue arrows and nearly vertical field lines. Both regimes contain working points of decoupling ratios $\frac{\Delta V_{FB}/\Delta H_x}{\Delta V_{FB}/\Delta H_z} \cong \frac{\Delta V_{FB}/\Delta H_z}{\Delta V_{FB}/\Delta H_x} \cong 10$, and exhibit typical dynamic working range of $10 - 20G$. Alternatively, two arbitrary points of fairly large gradients can be taken as working points, and the signal can be decoupled analytically. (b) An excellent H_x sensitive zone is identified, with decoupling ratio $\frac{\Delta V_{FB}/\Delta H_x}{\Delta V_{FB}/\Delta H_z} \geq 20$ and larger dynamic working range $(70 - 80G)$. These improved features are due to a smaller $(\cong 0.07\mu m^2)$ and more symmetric device.

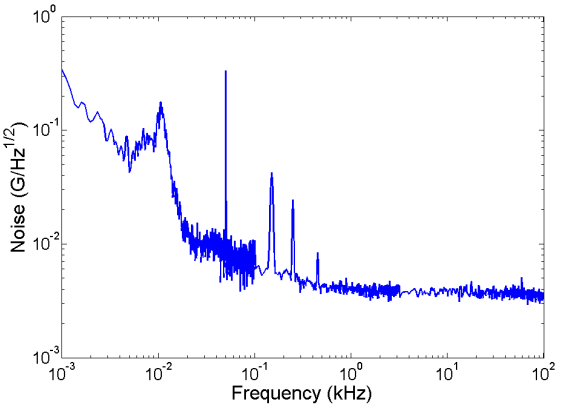

Figure 4.7: Field noise spectrum in a working point at 4.2 K. The field noise, taken at the x-sensitive point $H_x = 1650G$ and $H_z = 920G$, remains below $4\frac{mG}{\sqrt{Hz}}$ in the white noise regime.

vital that the sensitivity remains approximately constant in a sufficiently large range of fields. The required magnitude of this working range depends on the measured signal and should be larger than its expected variation. To address this issue we define the dynamic working regime as the regime around our working point at which the response can be considered as linear response, necessary for the reconstruction of the signal. This property is of acute importance in applications that locally deform the externally applied magnetic fields, e.g the Meissner effect in superconducting samples. On such applications, it is obvious that larger dynamic working regimes are in order, a property that can be achieved by further reduction of the tip size. Fig. 4.6 demonstrates the concepts of field decoupling and dynamic working range in two devices with typical sensitivity of few millivolts per gauss and dynamic working range of several tens of gauss. During our work we developed practical numerical tools that enabled us to quantify and compare sensitivity and linearity of working regimes.

Noise

To determine the typical signal-to-noise ratio of our device, we conducted systematic noise characterization of the $0.077\mu m^2$ 3JSOT. Fig. 4.7 shows its spectral noise density at an x-sensitive point with decoupling ratio $\frac{\Delta V_{FB}/\Delta H_x}{\Delta V_{FB}/\Delta H_z} \cong 10$. The noise profile consists of $1/f$ noise that changes after few tens of Hz into white noise smaller than $4\frac{mG}{\sqrt{Hz}}$ and remains unchanged at higher frequencies. To estimate the corresponding Φ^- noise level, we assume for simplicity that the device is symmetric and obtain a flux noise of $6\frac{\mu\Phi_0}{\sqrt{Hz}}$. In terms of spin sensitivity this noise level corresponds to $35\frac{\mu_B}{\sqrt{Hz}}$, which allows

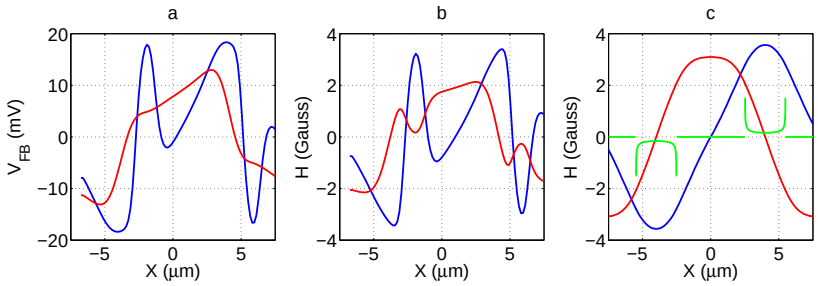

Figure 4.8: AC signal of line scan of the serpentine. A $15\mu m$ line scan applying AC current of 5mA in the serpentine. The estimated scanning height is $2\mu m$ and the field biases are $H_x = 114G$ and $H_z = 36G$ for the z-oriented point (red curve) and $H_x = 100G$ and $H_z = 36G$ for the x-oriented point (blue curve). See Fig. 4.6a for reference. (a) Raw data. (b) Alleged decoupled signal obtained by linear reconstruction. (c) Simulation, the green curve is the corresponding Meissner-like current density, and indicates the locations of the strips.

measuring very small magnetic moments in reasonable integration times. For example, it was shown by transport measurements that a single electron localized in a quantum dot on a carbon nanotube (CNT) has an in-plane magnetic orbital moment of $27\mu_B$ due to its precession around the CNT [24]. This means that combined with the high spatial resolution, such an electron can be detected using our device with integration time of few seconds.

4.2.2 Preliminary Results

As a demonstration we aimed towards imaging the current density in a Niobium serpentine, i.e many parallel superconducting strips that carry current in opposite directions. Close to one of the serpentine strips, this configuration is represented by the calculated curve plotted in Fig. 1.1b. As mentioned above, this particular sample imposes a considerable complication since we are driven out of our initial working point by the local field induced by the Meissner effect. Following the fabrication yield, the experiment sequence involves a lengthy process of cool-down, characterization and approach to imaging distance, still subjected to optimization. Only in three instances we saw features that clearly indicated that we are measuring non-trivial combinations of the in-plane and out-of-plane fields. Unfortunately, as our techniques are still inchoate, these attempts were ended by operational fault, such as crashing into the surface, before acquiring all the necessary data. This fact together with the Meissner problem prevented us from finally resolving a coherent measurement of the decoupled fields. In Fig. 4.8 we can see a good realization of our potential method and of its current shortcomings. In 4.8a we plot the raw signal we measure while biasing 5mA in the serpentine. We use a lock-in measurement to resolve only the

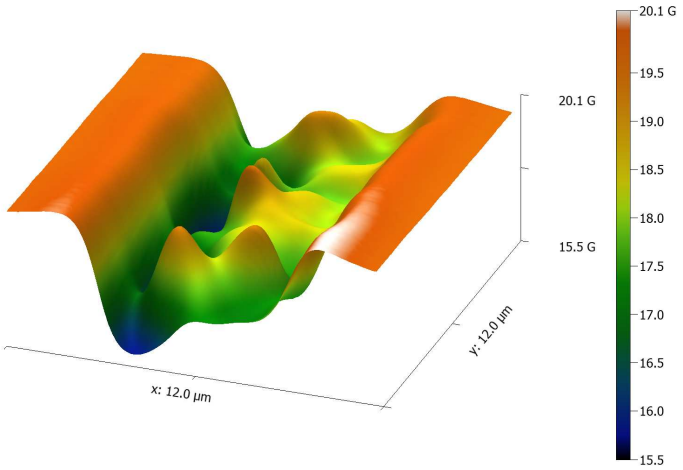

Figure 4.9: DC signal of $12 \times 12\ \mu m^2$ strip scan. the field bias is $H_x = 163G$ and $H_z = 86G$, see Fig. 4.6a for reference.

signal due to the AC current we apply. The data is acquired at two different working points associated with the response plotted in 4.6a. Both points exhibit poor decoupling ratio (< 10) but one of them resides at the base of the triangle and is more x-oriented (blue curve) and the other is more z-oriented (red curve). In Fig. 4.8b we plot the alleged analytically decoupled signal, H_x (blue) and H_z (red). Fig. 4.8c is a simulation that shows the calculated fields due to the 5mA biased current flowing in the serpentine. The scanning height is assumed 2µm, adequate to the measured signal. At this height we are not close enough so that the in-plane field will reflect the resolved local current density, but rather we see an integrated signal. The scanning width range was set to 15 µm, where each strip of the serpentine is 3 µm and the spacing between them is 5 µm. Inspecting the simulation one can identify a negative and positive H_x peaks at the center of each strip (± 4 µm) corresponding to the opposite current flows. This feature is present also in the raw data, but two opposite sharper peaks are disturbing the monotonous interpolation between them. The same is true for the H_z signal, it vanishes at two points, which we assume to be the centers of the the strips but is no longer symmetric as it should be. Namely, although the in-plane and out-of-plane features are present, they are far from being resolved. The signals obtained by the linear reconstruction process in 4.8b fail to show any noticeable improvement and thus confirm our suspicion: the device has been driven away from the predetermined working points by the relatively large DC fields generated by the sample.

We expected to extract better results from the second 3JSOT associated with the response plotted in 4.6b due to its significantly larger in-plane dy-

namic working range ($70-80\ G$) and decoupling ratio (≥ 20). Unfortunately, after completing one initial scan at a working point predominantly sensitive to the out-of-plane field, but with lower decoupling ratio (~ 5), we crashed into the surface before acquiring more data. Theses measurements were DC measurements, and no current was driven through the serpentine. In fig. 4.9 the shape of the serpentine is identified by the drop in the measured field, and vortex clusters are visible.

We conclude that until we achieve devices with larger dynamic working ranges (see section 5 below), imaging superconducting samples raises substantial difficulties. As a near future prospect, we consider other interesting samples in order to avoid this problem. Alternatively, we can try to produce a device sensitivite at zero out-of-plane field bias. This would be advantageous since for thin sample the surface screening currents due to the out-of-plane field induce an in-plane-field of comparable magnitude. An in-plane field bias, on the other hand, induces very little screening effect. Altogether, at zero out-of-plane bias the variation due to the Meissner effect should be small enough to allow us proper conditions to observe the current distribution signature.

5 Discussion

In this work we have described the fabrication, characterization and operation of a unique nanoSQUID which meets not only the size and sensitivity standards of the state of the art nanoSQUIDs, but also demonstrates tunable response to both in-plane and out-of-plane fields.

The main challenge that we currently face is lifting the restrictions imposed by the narrow accessible range of the field bias configuration. As mentioned above, instabilities in the measurement circuit give rise to large insensitive regions and in fact the major part of the interference pattern is presently not accessible for imaging purposes. This implies that we can work only in small regions, usually around the minimas, and only at a specific bias of fields. This problem is common to all SOT device, and a considerable effort is carried out in the lab in order to investigate its origins and tackle it. However in the 3JSOT context it is more acute, since its larger size implies smaller regions and due to the necessity of having two complimentary regions to decouple the fields. Until this challenge is met, we are limited to measure only signals with small variation (few tens of Gauss). Further reduction of the 3JSOT size should also be examined.

The 3JSOT has been proven reproducible with a good yield and the proper techniques and tools required to operate it were developed and optimized. This device is now an integral part of the experimental toolbox we acquired within the SOT scanning microscopy project, and we expect to see exciting physics with it. In particular we are interested in such applications where the signal contribution due to the in-plane field is advantageous, such as in-plane spin detection and transport current distribution in complex systems.

Appendix A: MoGe SOTs

Goals and Methods

In this appendix we briefly discuss a project that was carried out between July 2011 and March 2012 and was called down due to technical issues. The goal of this project was the fabrication and characterization of SOT based on amorphous Molybdenum-Germanium (α-MoGe) compound. The critical temperature of α-MoGe can be as high as 7 K, and decreases substantially for thin films [25]. To preserve the stoichiometry of the α-MoGe (we used 75at% Mo and 25at% Ge) thermal evaporation cannot be implemented, and typically MoGe films are produced by DC-sputtering technique. However, to impose SOT geometry, point source deposition is necessary, leading us to use pulsed laser deposition (PLD). Acquisition of this technique also triggers an opportunity for deposition of other superconducting compounds.

We worked with a Quanta-Ray-Series pulsed Nd:Yag Laser harmonic generator 1064nm- 266nm located at Ben Gurion University (BGU). The three-step self-aligned deposition was carried out in a vacuum chamber, using an adjusted rotatable holder. The base pressure was $\sim 10^{-6}$ Torr, but deposition in Ar ambient, at $10^{-3} - 10^{-5}$ Torr was also tested several times. Several preliminary attempts, resulting in full transitions in planar samples and partial transition in tips, encouraged us to install thickness monitor in the setup. The monitor was calibrated by measuring the thickness of planar samples by a ZYGO scanning white light interferometer. We designed a sealed container to cleanly carry the tips from BGU to the lab after we encountered several cases of contamination on them (Fig. 1 a). At a certain point we also introduced in-situ resistance measurement to the deposition process.

The main issue we had to address was improving the deposition rate. Higher rates result in high quality amorphous films, whereas rates comparable to the oxidation rate give rise to low quality material which is often not superconducting at all. The rate depends mainly on the power density on the target, which is dictated by the laser output power and the related optical elements. We found that rates of ~ 0.01 nm/sec or higher are sufficient in order to get superconducting films in this pressure. However, in this setup the laser and many optical elements were damaged, causing con-

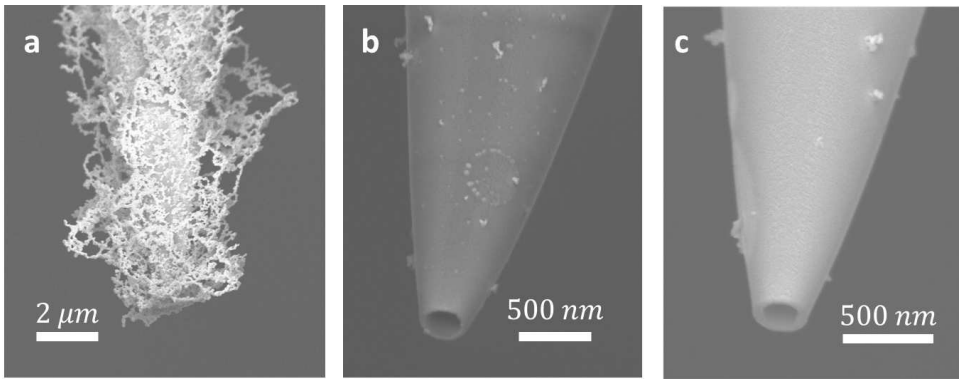

Figure 1: MoGe tips (a) Such contamination was observed on several tips before we used a sealed container to carry the tip from BGU to the lab. (b) MoGe tip. (c) MoGe tip that exhibited full transition at 4.2 K

stant degradation of the output power and therefore of the deposition rate. Moreover, the output power was highly unstable and often we had to manually align the harmonic generation crystals (HGC) between and even during depositions. When the rate finally decreased to ~ 0.005 nm/sec, and we stopped getting superconducting samples, we tried to improve the output power by replacing the Xenon pumping lamps of the laser. According to the technician that installed the new lamps, the damaged HGCs could not cope with the high power supplied by the new lamps and eventually were burnt out. Following this, the laser stopped working and we had to call down the project.

Results

SEM images of two tips with evaporated MoGe layer can be seen in Fig. 1 b and c. The amorphous nature of MoGe makes it a bit harder to distinguish between the superconducting electrodes and the quartz gap. The particulates at both images are frequently observed in laser ablated films due to clustering of the atoms, and in general can also harm the quality of the film. Figure 2 a shows the dependence of T_c as a function of thickness for several flat samples deposited at average rate of ~ 0.09 nm/sec. Deposition in Ar ambient in various pressures ($10^{-3} - 10^{-5}$ Torr) did not seem to have significant effect on the results. Fig 2 b presents transition of two MoGe evaporated tips. The blue curve corresponds to one of the first attempts, before we installed the thickness monitor in the chamber, so we do not know the exact rate. However, by measuring the thickness of a planar sample that was placed close to the holder we estimate that the rate was > 0.015 nm/sec and that 30 nm were evaporated on the leads and 15 nm on the ring, with a rotation of 110°. This tip exhibits only a partial transition from 11 kΩ

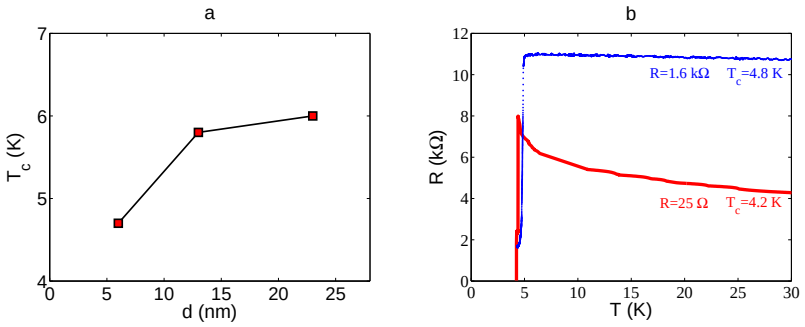

Figure 2: superconducting transition of MoGe (a) transition temperatures of several planar MoGe films as a function of their thickness. (b) full (red) and partial (blue) transitions of two MoGe evaporated tips. The final resistance and the transition temperature are indicated above the curves.

to 1.6kΩ at 4.8 K. The increase in the resistance as the sample is cooled down is a non-metallic property we observed in all the samples. The red curve corresponds to a tip that undergoes full transition above 4.2 K, and is imaged in Fig. 1 c Since this is a two-terminal measurement, we attribute the residual 25 Ω to the wire and contact resistance. 26 nm were evaporated on the leads and 24 nm on the ring with a rotation of 115° and in average rate of $0.01 - 0.015$ nm/sec, all in Ar ambient of 10^{-3} Torr. We could not, however, identify any field dependence in this tip. Soon after the fabrication of this tip the rate dropped tremendously to less than 0.005 nm/sec and we were not able to reproduce this result.

To conclude, we believe that these preliminary results indicate that with proper operational conditions, i.e. reliable high vacuum PLD system, it should be possible to realize a MoGe based SOT. The properties of such a device should then be characterized and studied, and potentially it may be another useful tool in the unique toolbox of the SOT sensors.

Bibliography

[1] S. J. Bending. Local magnetic probes of superconductors. *Advances in Physics*, 48(4):449–535, 1999.

[2] K. Hasselbach, D. Mailly, and JR Kirtley. Micro-superconducting quantum interference device characteristics. *Journal of applied physics*, 91(7):4432–4437, 2002.

[3] JR Kirtley, MB Ketchen, KG Stawiasz, JZ Sun, WJ Gallagher, SH Blanton, and SJ Wind. High-resolution scanning squid microscope. *Applied physics letters*, 66(9):1138–1140, 1995.

[4] N.C. Koshnick, M.E. Huber, J.A. Bert, C.W. Hicks, J. Large, H. Edwards, and K.A. Moler. A terraced scanning superconducting quantum interference device susceptometer with submicron pickup loops. *Applied Physics Letters*, 93(24):243101–243101, 2008.

[5] J. Nagel, OF Kieler, T. Weimann, R. Wolbing, J. Kohlmann, AB Zorin, R. Kleiner, D. Koelle, and M. Kemmler. Superconducting quantum interference devices with submicron Nb/HfTi/Nb junctions for investigation of small magnetic particles. *Applied Physics Letters*, 99(3):032506–032506, 2011.

[6] A.G.P. Troeman, H. Derking, B. Borger, J. Pleikies, D. Veldhuis, and H. Hilgenkamp. Nanosquids based on niobium constrictions. *Nano Letters*, 7(7):2152–2156, 2007.

[7] JR Kirtley. Fundamental studies of superconductors using scanning magnetic imaging. *Reports on Progress in Physics*, 73(12):126501, 2010.

[8] L. Hao, J. C. Macfarlane, J. C. Gallop, D. Cox, J. Beyer, D. Drung, and T. Schurig. Measurement and noise performance of nano-superconducting-quantum-interference devices fabricated by focused ion beam. *Applied Physics Letters*, 92(19):192507 –192507–3, may 2008.

[9] Y. Abulafia, Y. Wolfus, M. McElfresh, A. Shaulov, Y. Yeshurun, Y. Paltiel, H. Shtrikman, and E. Zeldov. Hall-array gradiometer for measurement of the magnetic induction vector in superconductors. *Journal of Applied Physics*, 85(8):5471–5473, 1999.

[10] A. Finkler, Y. Segev, Y. Myasoedov, M.L. Rappaport, L. Ne'eman, D. Vasyukov, E. Zeldov, M.E. Huber, J. Martin, and A. Yacoby. Self-aligned nanoscale squid on a tip. *Nano letters*, 10(3):1046–1049, 2010.

[11] A. Finkler, D. Vasyukov, Y. Segev, L. Ne'eman, EO Lachman, ML Rappaport, Y. Myasoedov, E. Zeldov, and ME Huber. Scanning superconducting quantum interference device on a tip for magnetic imaging of nanoscale phenomena. *Review of Scientific Instruments*, 83(7):073702–073702, 2012.

[12] EJ Romans, EJ Osley, L. Young, PA Warburton, and W. Li. Three-dimensional nanoscale superconducting quantum interference device pickup loops. *Applied Physics Letters*, 97(22):222506–222506, 2010.

[13] D.L. Tilbrook. Nanosquid sensitivity for isolated dipoles and small spin populations. *Superconductor Science and Technology*, 22(6):064003, 2009.

[14] E. Zeldov, J. R. Clem, M. McElfresh, and M. Darwin. Magnetization and transoprt currents in thin superconducting films. *Physical Review B*, 49:9802–9822, 1994.

[15] T. Schuster, H. Kuhn, EH Brandt, MV Indenbom, M. Kläser, G. Müller-Vogt, H.U. Habermeier, H. Kronmüller, and A. Forkl. Current and field pattern in rectangular and inhomogeneous superconductors. *Physical Review B*, 52(14):10375, 1995.

[16] R.B. Dinner, MR Beasley, and K.A. Moler. Cryogenic scanning hall-probe microscope with centimeter scan range and submicron resolution. *Review of Scientific Instruments*, 76(10):103702–103702, 2005.

[17] H.K. Onnes. Further experiments with liquid helium. c. on the change of electric resistance of pure metals at very low temperatures etc. iv. the resistance of pure mercury at helium temperatures. In *KNAW, Proceedings*, volume 13, pages 1910–1911, 1911.

[18] M. Tinkham. *Introduction to superconductivity*. International series in pure and applied physics. McGraw Hill, 1996.

[19] U. Essmann and H. Träuble. The direct observation of individual flux lines in type ii superconductors. *Physics letters A*, 24(10):526–527, 1967.

[20] B.D. Josephson. Possible new effects in superconductive tunnelling. *Physics Letters*, 1:251–253, 1962.

[21] R.P. Feynman, R.B. Leighton, and M.L. Sands. *The Feynman Lectures on Physics: Quantum mechanics*. The Feynman Lectures on Physics. Addison-Wesley, 1965.

[22] M.E. Huber, P.A. Neil, R.G. Benson, D.A. Burns, AF Corey, C.S. Flynn, Y. Kitaygorodskaya, O. Massihzadeh, J.M. Martinis, and GC Hilton. Dc squid series array amplifiers with 120 mhz bandwidth (corrected). *Applied Superconductivity, IEEE Transactions on*, 11(2):4048–4053, 2001.

[23] John Clarke and Alex I. Braginski, editors. *The SQUID Handbook*. Wiley-VCH, Weinheim, 1 edition, 2004.

[24] F. Kuemmeth, S. Ilani, DC Ralph, and PL McEuen. Coupling of spin and orbital motion of electrons in carbon nanotubes. *Nature*, 452(7186):448–452, 2008.

[25] J. Cuppens. *Confinement Effects of the Condensate and Flux in Nanostructured Superconductors*. PhD thesis, Catholic university of Leuven, November 2011.